JOURNAL OF AIRCRAFT
Vol. 33, No. 2, March–April 1996

Body-Axis Rolling Motion Critical States of a 65-Degree Delta Wing

Jerry E. Jenkins* and James H. Myatt†
U.S. Air Force Wright Laboratory, Wright–Patterson Air Force Base, Ohio 45433-7531
and
Ernest S. Hanff‡
Institute for Aerospace Research, Ottawa, Ontario K1A 0R6, Canada

Dynamic wind-tunnel test results of a 65-deg swept delta wing are reviewed. These tests involved body-axis rolling motions at moderate (15- to 35-deg) angles of attack in both the Institute for Aerospace Research 2 × 3 m low-speed wind tunnel and the 7 × 10 ft Subsonic Aerodynamic Research Laboratory facility at Wright–Patterson Air Force Base. They included static, forced oscillation, and free-to-roll experiments with flow visualization. Multiple trim points (attractors) for body-axis rolling motions and other unusual dynamic behavior were observed. These data are examined in light of the nonlinear indicial response theory. The analysis confirms the existence of critical states with respect to roll angle. When these singularities are encountered in a dynamic situation, large and persistent transients are induced. Conventional means of representing the nonlinear forces and moments in the aircraft equations of motion, notably the locally linear model, are shown to be inadequate for these cases. Finally, the impact of these findings on dynamic testing techniques is discussed.

Nomenclature

b = wingspan, ft
C_l, C_m = body-axis rolling moment and pitching moment coefficients, nondimensionalized with respect to qSb and $qS\bar{c}$, respectively
$C_{l,\mathrm{dyn}}$ = dynamic rolling moment coefficient, $C_l(t) - C_{l,\mathrm{stat}}$
$C_{l,\mathrm{stat}}$ = static rolling moment coefficient, i.e., equilibrium C_l corresponding to the instantaneous value of roll angle
$C_{l_\phi}(t)$ = nonlinear rolling moment indicial response, due to step input in roll angle
$\bar{c}$ = mean aerodynamic chord, ft
k = reduced frequency, $\omega b/2U_\infty$
q = freestream dynamic pressure, lb/ft^2
Re = Reynolds number
S = wing area, ft^2
t = time, s
U_∞ = freestream velocity, ft/s
x_{vb} = vortex breakdown position, fraction of root chord aft of wing vertex
ξ = running time variable denoting motion history, $-\infty \leq \xi \leq \tau$, s
σ = total angle of attack, body-axis inclination with respect to U_∞, deg
τ = time at step onset, s
ϕ = body-axis roll angle, deg
ϕ_0 = initial roll angle for free-to-roll experiments, also mean roll angle for harmonic motion experiments
ω = circular frequency, rad/s

Presented as Paper 93-0621 at the AIAA 31st Aerospace Sciences Meeting, Reno, NV, Jan. 11–14, 1993; received Sept. 14, 1994; revision received Aug. 29, 1995; accepted for publication Aug. 31, 1995.

*Aerospace Engineer, WL/FIGC 2210 Eighth Street, Suite 21. Senior Member AIAA.
†Aerospace Engineer, WL/FIGC 2210 Eighth Street, Suite 21. Member AIAA.
‡Senior Research Officer, Applied Aerodynamics Laboratory. Member AIAA.

Introduction

DYNAMIC coupling between aircraft motion and aerodynamic forces and moments acting on the aircraft is at the heart of stability and control. Maintaining sufficient fidelity in aerodynamic models for these interactions has become an increasingly difficult problem in the face of flight envelope expansion.

A theoretical method for studying the nonlinear aspects of the flight dynamics problem has been under development by Tobak[1] and his colleagues since the 1960s. Their initial approach[2] introduced two important new concepts: 1) a nonlinear indicial response and 2) a generalized superposition integral. As with linear indicial response methods, the idea is to represent aerodynamic responses (force or moment) due to arbitrary motion inputs as a summation of responses to a series of step motions. The nonlinear indicial response, as opposed to its linear counterpart, accounts for changes induced by the motion history leading up to step onset.

Subsequently, results from the growing body of nonlinear dynamical system theory were used to greatly strengthen the model.[3,4] The key idea of these extensions has been to accommodate the existence of critical states, i.e., specific values of the motion variables where discrete changes in static aerodynamic behavior occur. These are singular points that require special handling in the superposition integral. Critical states are important because potentially large and persistent transient aerodynamic effects can be anticipated when an aircraft encounters them in a dynamic situation.

Truong and Tobak[5] have also demonstrated that, for static aerodynamic characteristics that are time invariant, the nonlinear indicial response, together with the generalized superposition integral, can be derived directly from the Navier–Stokes equations. Thus, the theory has a sound mathematical basis and captures the flow physics as well. There is still much work to be done, especially for cases involving time-dependent equilibrium states. Nevertheless, the theory is rich in its ability to represent a wide range of important aerodynamic nonlinearities that can be encountered in maneuvering flight.

Independently, Hanff[6] proposed the reaction hypersurface model. As opposed to the time-domain indicial response model, the hypersurface is expressed in terms of a set of in-

dependent variables consisting of the instantaneous values of the motion variables and their time derivatives. It was, at its inception, designed to be experimentally based and primarily intended for simulations of aircraft motion in nonlinear settings where the classical stability derivative approach breaks down.[7] More recent work[8] has been aimed at establishing the theoretical connection between the reaction hypersurface and nonlinear indicial response models.

Experiments designed to study either of these mathematical models demand a dynamic test capability that can efficiently collect the necessary nonlinear and time-dependent data. A large-amplitude high-rate roll oscillation system,[9] developed at the Canadian Institute for Aerospace Research (IAR), meets this requirement.

Hanff and Jenkins[10] used this rig to study the roll dynamics of both a 65-deg delta wing and an 80–65-deg double-delta wing at the IAR. Their experiments produced some extremely interesting results that require further explanation.

The 65-deg delta wing configuration was found to have multiple stable trim points in roll (depending on roll-axis inclination) as reported by Hanff and Ericsson.[11] Locations for these attractors are repeated here in Table 1. They argue (based on analysis of static rolling-moment data at $\sigma = 30$ deg) that asymmetric vortex breakdown, induced by differing effective sweep angles on each wing panel, is the root cause. However, the dynamic behavior observed in free-to-roll experiments is harder to explain, although Hanff and Huang[12] have shown that the instantaneous loads are largely driven by the dynamics of leading-edge vortex breakdown.

In free-to-roll tests, the model is given an initial roll displacement, then released by disengaging a remotely actuated clutch. The model is then free to roll about its body axis, restrained only by a small amount of bearing friction in this degree of freedom. The inertia of the moving system was adjusted to ensure that the free-to-roll responses were in the same frequency range as the dynamic force measurements (about 7.7 Hz, see Table 2). Since frequency is inversely proportional to the reference length at fixed flight speed, corresponding full-scale vehicle frequencies are realistic.

Two free-to-roll time histories for the 65-deg configuration at $\sigma = 30$ deg, plotted in the phase plane, are shown in Fig. 1. Note that the trajectory for the −58.3-deg release angle (solid curve) finds the stable equilibrium point at about 0-deg roll, while the 53.1-deg release trims at about 21 deg. Both trajectories pass quite close to attractors (21 and 0 deg, respectively) with very low rates, but do not trim there. This behavior was highly repeatable. Furthermore, the trajectories intersect at several points. Similar intersections of phase-plane trajectories (for wing-rock motions) have been observed only when vortex breakdown occurs over the wing.[13] Clearly, some phenomenon, not explicitly accounted for in the two-dimensional phase-plane representation, affects the motion. Persistent motion history effects, perhaps related to vortex breakdown dynamics, that require more than a knowledge of the instantaneous roll angle and roll rate are a strong possibility.

Finally, forced-oscillation motions about a zero mean roll angle produce distinctly different rolling-moment responses than those measured for motions with mean roll angles of 7 deg or greater.[10] An analysis of the static and dynamic force data[8] suggested that this behavior can be explained by the existence of critical states. Indeed, large transient effects (with the magnitudes of the static and dynamic effects being of the same order) were noted in the response following encounters with the suspected critical states. These transients persist for at least a quarter cycle at $k = 0.08$.

Follow-on tests, designed to investigate the cause of the behavior noted earlier, were conducted in the Subsonic Aerodynamic Research Laboratory (SARL) wind tunnel at Wright–Patterson Air Force Base. An analysis of the static, dynamic, free-to-roll, and flow visualization data taken during these experiments is presented later. Relevant aspects of critical-state theory are discussed and data confirming the existence of roll-motion critical states are presented. The impact on dynamic testing techniques (including data collection and reduction) and application to the simulation and analysis of the flight dynamics problem are addressed in this article's final sections.

Table 1 Roll attractor locations

Angles, deg	
Sting	Roll
20	0
25	±1.5
30	0, ±21
35	±11
40	0

SARL Experiments

IAR's high-amplitude, high-rate roll apparatus was also used in the SARL tests. A comprehensive experimental program involving over 800 runs was conducted using the 65-deg delta-wing configuration (Fig. 2). The test matrix is summarized in Table 2.

Since SARL is an open-return atmospheric tunnel, the IAR Mach number, Reynolds number, and reduced frequencies could not be matched simultaneously. However, test conditions were chosen to match those at the IAR as closely as possible. In addition, the model support systems and tunnel cross-section geometry are quite different in the two tunnels. Thus, the

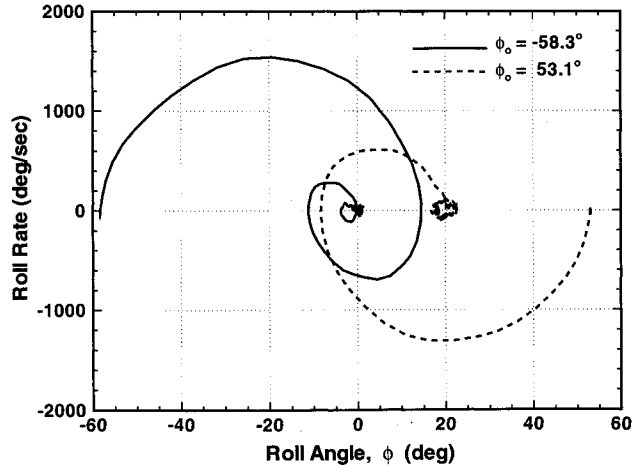

Fig. 1 Free-to-roll motions: $\sigma = 30$ deg.

Table 2 SARL test conditions

Test type	Roll offset, deg	Amplitude, deg	Frequency, Hz	Total angle of attack, deg
Static force	−70–70	NA	NA	15, 30, 35
Dynamic force	0–42	5–40	1.1, 4.4, 7.7	15, 30, 35
Free-to-roll	−65–65	NA	7.7	30, 35
Flow visualization	0–42	5–40	0, 1.1, 4.4, 7.7	30, 35
Surface pressure	0–42	5–40	0, 1.1, 2.2, 4.4, 7.7	15, 30, 35

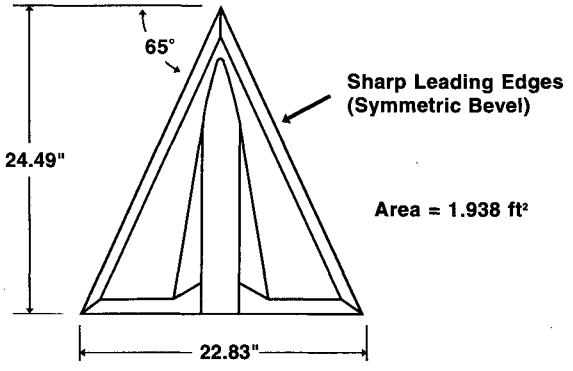

Fig. 2 Model geometry.

very good facility-to-facility repeatability eliminated the possibility of significant support and wall interference effects.

Dynamic force and moment measurements were taken with the model forced in constant amplitude harmonic motion. Data were taken at 4.4 and 7.7 Hz (k = 0.08 and 0.14) to match IAR conditions. These results closely tracked static measurements except when the motion passed through small roll angles.[8] Thus, in the SARL experiments, dynamic tests were also conducted at 1.1 Hz (k = 0.02) to determine how the extremely large dynamic effects, incurred at small roll angles, approach quasisteady behavior at low reduced frequency.

Laser-sheet flow visualization data and unsteady surface pressure measurements were also taken. Thus, an extensive data set was created that allows a coordinated study of vortex dynamics (including breakdown) and the resulting unsteady aerodynamic forces and moments.

Free-to-roll experiments were also repeated in the SARL tunnel. These data provide an independent check on the accuracy of the dynamic force measurements (and the mathematical model used to represent them) since the measured forces, together with the known model and test-rig inertia, can be used to predict the free-to-roll motion.

Critical States, Theoretical Basis

A development of the nonlinear indicial response and critical states[1,3,4] is beyond the scope of this article. However, some key results, pertinent to the present discussion, are summarized:

1) The nonlinear indicial response (NIR) is represented mathematically as a functional to incorporate the motion history effect.

2) The NIR is a derivative, called the Fréchet derivative, of the functional representing an aerodynamic response in terms of its motion history. It is the limit, as step height goes to zero, of the incremental response (due to the step input) divided by step height. Following Tobak's notation,[1] the rolling moment due to an infinitesimal step in roll angle is written

$$C_{l_\phi}(t) = C_{l_\phi}[\phi(\xi);\, t,\, \tau]$$

where square brackets denote a functional; the first argument is the independent function defining the motion history (roll angle in this case); and arguments following the semicolon give, respectively, the times at which 1) the response is to be evaluated (observed) and 2) the step motion was initiated.

Therefore, the function $\phi(\xi)$ is to be interpreted as the motion history from $t = -\infty$ to step onset τ, and the motion is to be held constant at $\phi(\tau)$ thereafter. The long-term behavior of the aerodynamic response functional (after transients due to the motion have died away) is called the equilibrium state.

3) If the Fréchet derivative exists everywhere on a time interval (i.e., for the range of motion variables encountered on that interval), the generalized superposition integral may be used to construct the net aerodynamic response (rolling moment in this case) over the interval. Thus,

$$C_l(t) = C_l[\phi(\xi);\, t,\, 0] + \int_0^t C_{l_\phi}[\phi(\xi);\, t,\, \tau]\,\frac{d\phi}{d\tau}\,d\tau$$

Following the notation introduced previously, the first term on the right-hand side (RHS) is the rolling moment at time t resulting from the roll-angle variation $\phi(\xi)$, which is the motion history prior to $\xi = \tau = 0$, and is held constant at $\phi(0)$ for all $\xi \geq 0$. The functional in the second term is the NIR, as defined earlier. In this case, τ is the variable of integration and the time at step onset. Thus, the integral sums the effects of all indicial responses over the interval 0 to t.

4) If, on the other hand, there are specific points τ_c within the interval where Fréchet differentiability is lost (at a critical state ϕ_c), the integration may not be carried beyond the instant at which a critical state is encountered without acknowledging the existence of the singularity.

5) Loss of Fréchet differentiability is handled by allowing the equilibrium response to change discretely to a new state. Thus, the integral must be split to isolate the critical state, i.e.,

$$C_l(t) = C_l[\phi(\xi);\, t,\, 0] + \int_0^{\tau_c-\varepsilon} C_{l_\phi}[\phi(\xi);\, t,\, \tau]\,\frac{d\phi}{d\tau}\,d\tau + \int_{\tau_c+\varepsilon}^{t} C_{l_\phi}[\phi(\xi);\, t,\, \tau]\,\frac{d\phi}{d\tau}\,d\tau + \Delta C_l(t;\, \phi_c) \tag{1}$$

where

$$\Delta C_l(t;\, \phi_c) = C_l[\phi(\xi);\, t,\, \tau_c + \varepsilon] - C_l[\phi(\xi);\, t,\, \tau_c - \varepsilon] \tag{2}$$

ΔC_l, as given by Eq. (2), is the transient response associated with ϕ_c. Note that it depends on the motion history from $-\infty$ to just beyond τ_c. However, its effect persists for times $t > \tau_c$.

6) Fréchet differentiability may be lost in several ways.[1] A very important case is when time-invariant equilibrium flows lose their analytic dependence on a motion parameter (body-axis roll angle in these experiments). There are at least two ways this can happen, both involving an exchange of stability among competing equilibrium flows:

a) Static aerodynamic responses (i.e., responses corresponding to solutions of the time-invariant form of the Navier–Stokes equations) can develop a fold at a critical value of the motion parameter, possibly an indirect result of a subcritical bifurcation. The response slope becomes infinite at the fold, invalidating the Fréchet derivative. Note that a subcritical bifurcation requires the existence of multiple (nonunique) steady-state solution curves on both sides of the parameter's critical value.[14] However, there is an exchange of stability among the available branches at the critical value. The initial or basic solution becomes unstable when the parameter is greater than the critical value. Any perturbation will force a transition to a new (and stable) equilibrium flow. The transition is seen as a discontinuous jump when plotted vs the motion parameter; however, its time history is given by Eq. (2).

b) Static aerodynamic responses can experience a supercritical bifurcation at a critical value of the motion parameter. Response-curve slopes become discontinuous at such points, again invalidating the Fréchet derivative. Nonunique steady-state solution curves are required in this case also.[14] The apparent discontinuous jump in slope is caused by a transition from the unstable basic solution to an intersecting (stable) equilibrium-solution curve as the motion parameter passes through the critical value. In general, the intersecting solution curves are smooth.

7) Changes in flow topology (a change in the number of singular points in either the external flow or in skin-friction lines) when the motion parameter reaches a critical value may signal the loss of Fréchet differentiability. Tobak et al.[1] anticipate that equilibrium responses could cease to be analytically dependent on the motion parameter at such points. They also state that there could also be "a significant increase in the time required for the ... response to reach a new equilibrium state."

NIR theory, as outlined previously, is used extensively to interpret the new experimental results. However, there are important restrictions implicit in the analysis. Static force data have been time averaged to remove the effects of model and/or sting vibrations, freestream fluctuations, etc., and also to stay within the NIR theoretical framework (which in its current form requires time-independent equilibrium states). Furthermore, the relationship between time-averaged force and moment behavior and topology changes in the corresponding mean flow deserves closer scrutiny since it is highly desirable to have definitive experimental evidence pointing to critical state locations. Therefore, the potential impact of time-averaging and mean-flow topology changes are examined in the following section. This is done by using a well-known flow as an example. In this case, the parameter controlling the flowfield evolution is Reynolds number (as opposed to an evolution with respect to a motion variable as discussed earlier).

Flow About a Cylinder

Consider the two-dimensional flow about a circular cylinder at Reynolds numbers ranging from zero to values beyond the onset of vortex shedding. As Re is increased from zero, the force balance (initially between only pressure and viscous forces) must accommodate the increasing effects of inertial forces. At very low Reynolds numbers, the flow remains fully attached to the cylinder (as shown in Fig. 3a); the flowfield topology is characterized by two half-saddle points[15] located at the fore and aft stagnation points on the plane of symmetry. A separation bubble appears at $Re \approx 7$ (based on the cylinder diameter) as shown in Fig. 3b. Associated with the bubble are three half-saddle points on the surface (an increase of two) plus a saddle point in the downstream flowfield that provides closure for the bubble. In addition, there are two nodes (degenerate foci, also called centers) that account for the closed streamlines within the bubble. Thus, both flows (with and without the standing eddies) conform to the topological rule[15] for the flow in a planar slice through a body:

$$\left(\sum_N + \frac{1}{2}\sum_{N'}\right) - \left(\sum_S + \frac{1}{2}\sum_{S'}\right) = -1$$

where Σ_N and Σ_S denote the number of nodes and saddle points, respectively, in the flowfield and $\Sigma_{N'}$ and $\Sigma_{S'}$ are the number of half-nodes and half-saddle points on the body surface, respectively.

Thus, there is a distinct change in flowfield topology at $Re \approx 7$ (going from two topological singularities to a total of seven, including three off-surface singularities). However, the changeover is perfectly smooth. There are no competing (nonunique) equilibrium solutions for $7 < Re < 50$; i.e., the topological change does not involve a flowfield instability and the possibility of a supercritical bifurcation must be ruled out. However, the appearance of separated flow behind the cylinder implies the existence of reverse-flow velocity profiles that are more susceptible to instability.

At a $Re \approx 50$, the flow within the bubble does become unstable and vortex shedding begins. The resulting equilibrium flow is time periodic, but there is a time-invariant mean flow. Numerous calculations for the steady flow in this Re range have been published.[16] However, experiments by Nishioka and Sato[17] (Fig. 4) clearly show that the separation bubble corresponding to the time-invariant mean flow when vortex shedding is present is very much shorter than it would have been in the absence of fluctuations. Furthermore, the change in bubble length begins abruptly at the critical Re (corresponding to the onset of shedding), and entails a discontinuous slope with respect to Re. A corresponding discontinuous change in the slope of the integrated load, i.e., the mean drag, should also be expected.

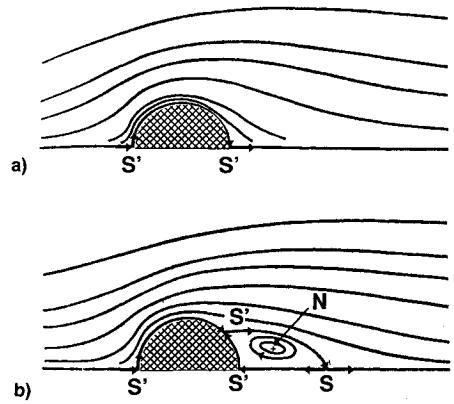

Fig. 3 Steady flow about a cylinder: a) attached flow, $Re < 7$ and b) with separation bubble, $Re > 7$.

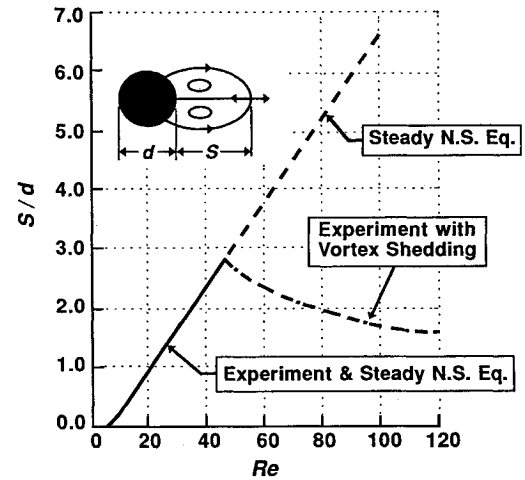

Fig. 4 Separation bubble length vs Re with and without unsteady vortex shedding.

Note that there has been no change in the number and types of topological singularities present in the mean flow at $Re \approx 50$ (although significant changes in topology are evident if the flowfield is frozen at any instant). Thus, two time-invariant equilibrium solutions are available above $Re \approx 50$, corresponding to the cases with and without vortex shedding. Therefore, the onset of a time-periodic equilibrium condition is seen as a supercritical bifurcation of the mean flow wherein the long bubble solution loses its stability. However, there is no corresponding change in mean-flow topology.

Recent computations by Chen et al.[18] strongly support the notions that 1) there are no bifurcations associated with the appearance of the separation bubble and 2) loss of stability in the steady flow, through a Hopf bifurcation, is associated with the onset of unsteady vortex shedding.

Thus, the conclusions are as follows:

1) Under normal conditions (only one equilibrium solution) a change in mean-flow topology cannot imply a loss of Fréchet differentiability; i.e., there is no corresponding critical state.

2) Supercritical bifurcations of the mean flow can occur (a critical state) without a coincident change in mean-flow topology when the equilibrium flow becomes time dependent.

3) The significance of a topological change in the mean flow is that if inflexive velocity profiles are created, then the resulting mean flow is more susceptible to instability.

These observations having been made, the discussion now returns to the rolling delta wing.

Experimental Evidence

Based on the theory presented previously, aerodynamic data in the presence of critical states should exhibit the following traits:

1) Static (fixed vehicle attitude) flow visualization studies may show a change in flow structure at a critical state. If the visualization technique implicitly involves time averaging (e.g., oil-flow studies of skin-friction lines), a topology change is neither necessary nor sufficient for the existence of a critical state. However, a mean-flow topology change can indicate a susceptibility to instability and may be closely associated with a subsequent critical state, especially if flowfield variables (such as pressure gradient) are highly sensitive to small changes in the parameter.

2) Static force and moment data should exhibit nonanalytic behavior across critical states; i.e., there should be a discontinuity in the variation of the force data and/or their derivatives with respect to the motion variable if the equilibrium flow is time invariant. The discontinuity is located at the critical state. If the equilibrium response is not time invariant, a discontinuity may still be apparent in the mean (time-averaged) loads, as in the example presented earlier. This latter possibility is a likely consequence of the basic flow becoming unstable, thereby sending the unsteady equilibrium solution on a new and stable path.

3) Transient effects should be observed following dynamic critical-state encounters. The transient, ΔC_l in Eqs. (1) and (2), will in general depend on motion history.

SARL data (for the rolling 65-deg delta wing) pertinent to each attribute are discussed later. All data discussed here were taken at the same condition (0.3 Mach number and σ = 30 deg). For these discussions, the term static refers to the model being held fixed (within normal experimental constraints) with respect to the freestream and does not imply a time-invariant equilibrium state. All measurements taken under static conditions are time-averaged unless explicitly stated to be otherwise.

Static Flow Structure

Equilibrium vortex breakdown locations for the left wing as a function of static roll angle, from Hanff and Huang,[12] are shown in Fig. 5. (For positive roll angles, the left wing is on the lee side; i.e., it has been rolled away from the freestream velocity vector. Conversely, it is the windward wing for negative roll angles.) The solid line is a linear least-square-error fit to the circular data points (correlation coefficient 0.996). Note that the experimental point at ϕ = 5 deg (triangle) departs significantly from the linear fit. Thus, in agreement with Hanff and Huang's interpretation of Wentz's[19] data, breakdown location is seen to be a nonlinear (perhaps discontinuous) function of static roll angle in the 4- to 5-deg range. For ϕ greater than 5 deg the breakdown point is well aft of the trailing edge. In addition, vortex breakdown reaches the vertex at about ϕ = −13 deg, as suggested by the linear extrapolation. When the leading-edge vortex structure on both wings is considered, the conditions $|\phi| \approx 5$ and 13 deg are candidate critical states.

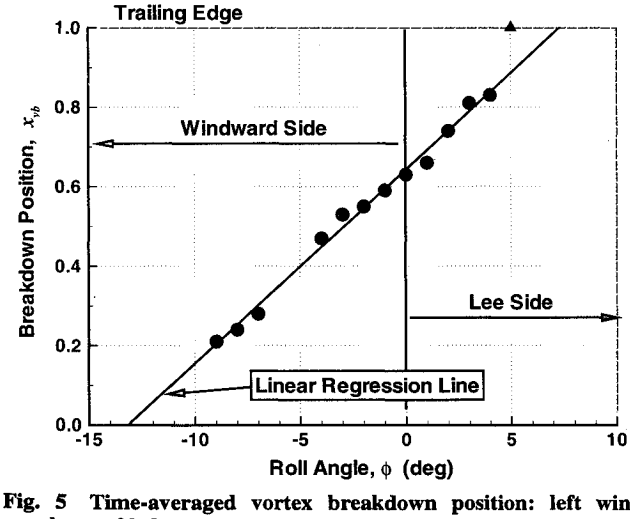

Fig. 5 Time-averaged vortex breakdown position: left wing panel, σ = 30 deg.

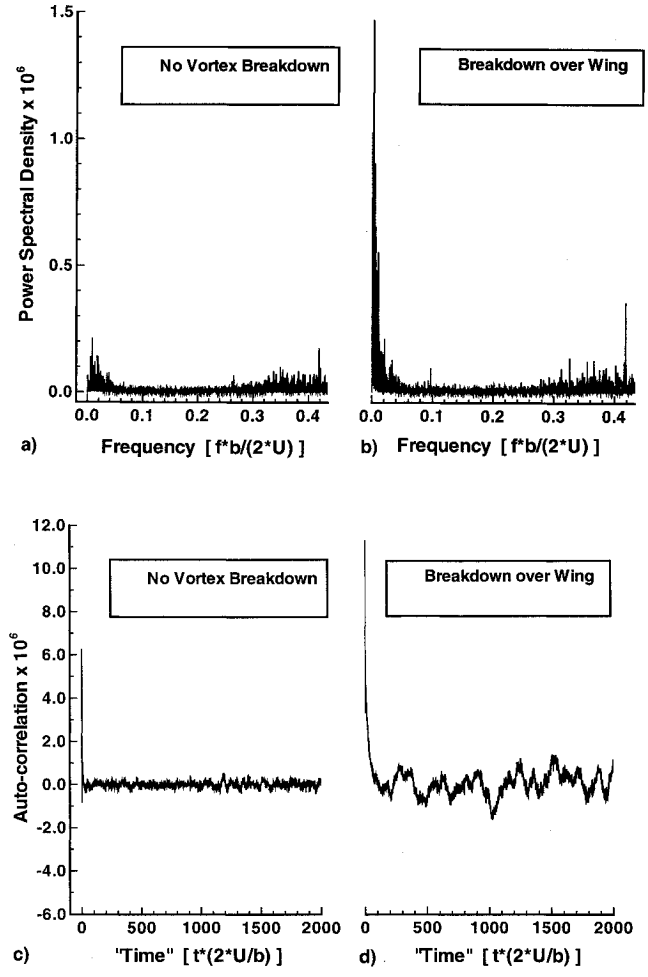

Fig. 6 Rolling-moment coefficient power spectral density: a) ϕ = 20 and b) 5 deg; and rolling moment coefficient autocorrelation: c) ϕ = 20 and d) 5 deg.

The first, $|\phi| \approx 5$ deg, may be a critical state principally because a discontinuous rearward shift of the breakdown point on the lee wing would cause a jump (increase) in the equilibrium lifting pressures on that side (aft of about 80% chord from Fig. 5). Any discontinuities in the forces (or their derivatives) with respect to ϕ would, of course, invalidate the Fréchet derivative. Time-averaged static force data supporting this view are discussed later.

Secondly, $|\phi| \approx 13$ deg is almost certainly a critical state because, if the breakdown point reaches the vertex, the stagnation point in the vortex-core axial flow[20] is lost. The precise roll angle where this occurs is unknown due to flow visualization difficulties that require an extrapolation of the data to the apex. However, the breakdown point will unquestionably reach the vertex for a sufficiently large roll angle.

Static Force and Moment Behavior

Unsteady aerodynamic force and moment measurements, taken under static conditions where vortex breakdown is ab-

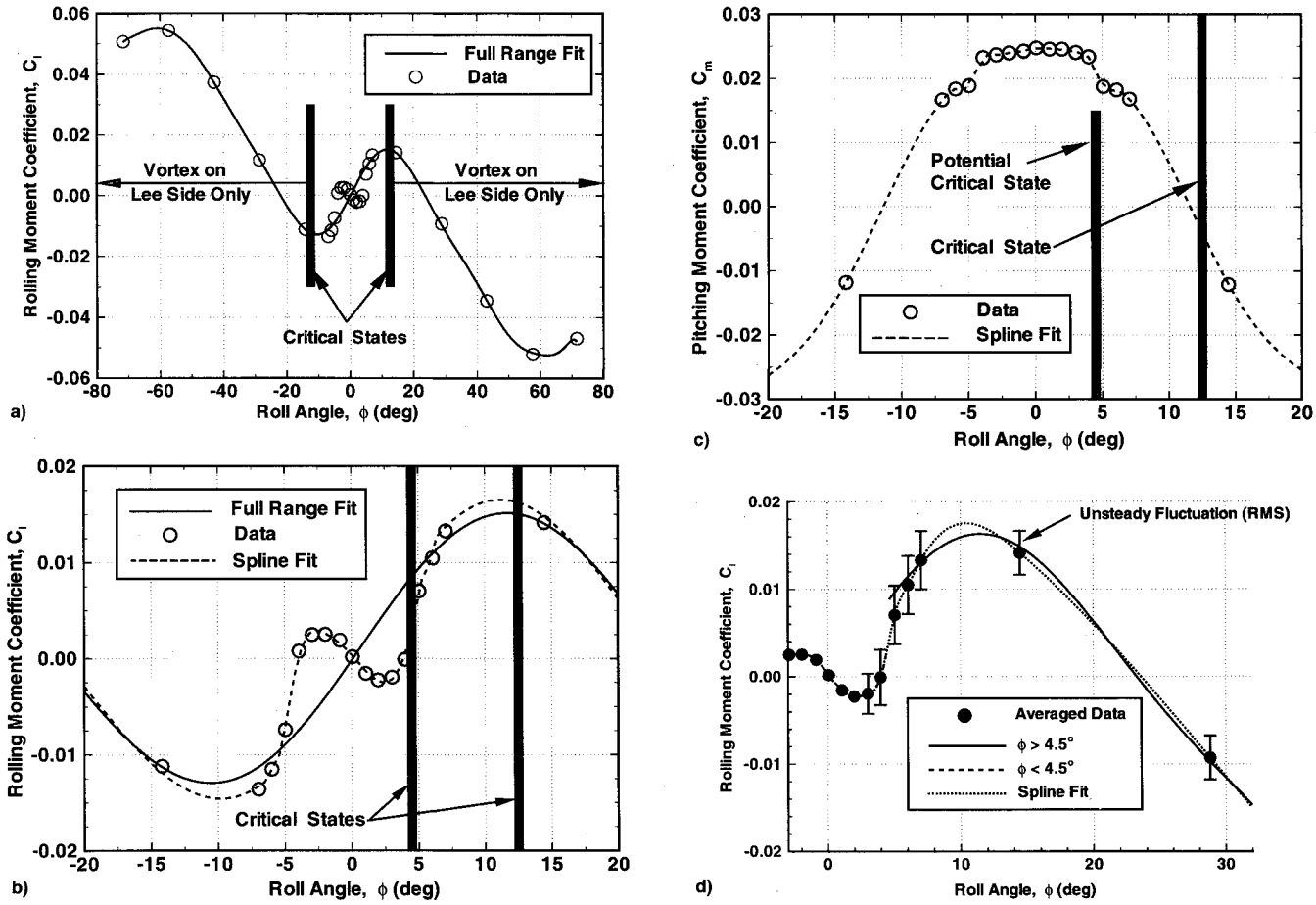

Fig. 7 a) Static (time-averaged) rolling-moment coefficient data, σ = 30 deg; b) full-range polynomial fit to rolling-moment data: σ = 30 deg, $|\phi| < 20$ deg; c) time-averaged pitching-moment coefficient data: σ = 30 deg, $|\phi| < 20$ deg; and d) polynomial fits for the ranges $|\phi| < 4.5$ deg and $|\phi| > 4.5$ deg.

sent, are characterized by relatively small, broad-band, random fluctuations about a well-defined mean value. (Mean values calculated for overlapping 13-s samples repeat quite well.) Power-spectral density (PSD) and autocorrelation plots for the rolling-moment coefficient for such a case (σ = 30 deg, ϕ = 20 deg) are presented in Figs. 6a and 6c. When vortex breakdown is near the trailing edge of the left wing and at about 40% root chord on the right wing, σ = 30 deg and ϕ = 5 deg, there is a marked increase in the low-frequency content of the PSD (Fig. 6b), i.e., for nondimensional frequencies, $(f\ b)/(2U_\infty)$, less than about 0.04. As a result, the rms value of the fluctuations goes from 0.0025 to 0.0033 (a 32% increase) and the autocorrelation, Fig. 6d, takes on a distinctly quasiperiodic appearance.

Time-averaged static rolling-moment coefficient vs roll angle is presented in Fig. 7a. Also shown are the critical states locations corresponding to the loss of a coherent vortex on the windward wing (breakdown reaches the vertex). The degree of unsteadiness, in terms of the rms value of the fluctuations about the mean, is shown by error bars in Fig. 7d.

If critical states exist in the roll-angle range tested, then the function representing the rolling moment (or any other force/moment) cannot be analytic. Given only values for a function at a discrete number of points, it is impossible to prove that it is (or is not) an analytic function. However, a cursory investigation of its behavior is worthwhile.

If a function is analytic it can be represented by a Taylor series. Therefore, a stepwise regression analysis was used to look for a polynomial (least-squares fit) representing C_l as a function of ϕ since the polynomial can be interpreted as a truncated Taylor series. Thirty-two terms (each an odd Legendre polynomial[21]) were included in the list of possible contributors to the regression equation. Test data points were interpolated (with a cubic spline) at 255 points distributed in a geometric sequence beginning at the origin and increasing in either direction; i.e., the ratio of ϕ_{i+1} to ϕ_i was held constant. The proportionality constant between successive interpolation points was systematically varied such that intervals between successive points ($\phi_{i+1} - \phi_i$) at the extremes ranged from 2 to 40 times the interval at the origin $\phi_1 - \phi_0$. This was done to give additional weight to points near the origin, where the rolling moment is rapidly varying, while keeping enough density at the extremes to prevent the polynomial from oscillating. Values between 30–40 were used in the final results discussed later.

The solid curve (labeled Full Range Fit) in Fig. 7a is the polynomial fit over the complete roll-angle range. Thirteen terms were included in the final regression equation; the rest were rejected because they offered no improvement in the correlation. Note that the stable trim point at ϕ = 0 deg was not captured despite the heavy emphasis given to points in this region (160 of 255 points were within $|\phi| < 16$ deg). However, this result may be influenced by a gap in test data coverage on either side of the critical state at about 13 deg (raising questions about the validity of the spline fit in this region). Further static testing is required to determine the actual behavior.

An expanded view of the region -20 deg $\leq \phi \leq 20$ deg is presented in Fig. 7b. Also shown is the cubic spline fit and the possible critical state at $\phi \approx 5$ deg (from flow visualization results). Note the separation of data points for $|\phi| \leq 4$ deg and for 5 deg $\leq |\phi| \leq 7$ deg. Moreover, Fig. 7c (pitching moment vs roll angle) reinforces the notion that there is a discontinuity between the two groups. Both effects, a nose

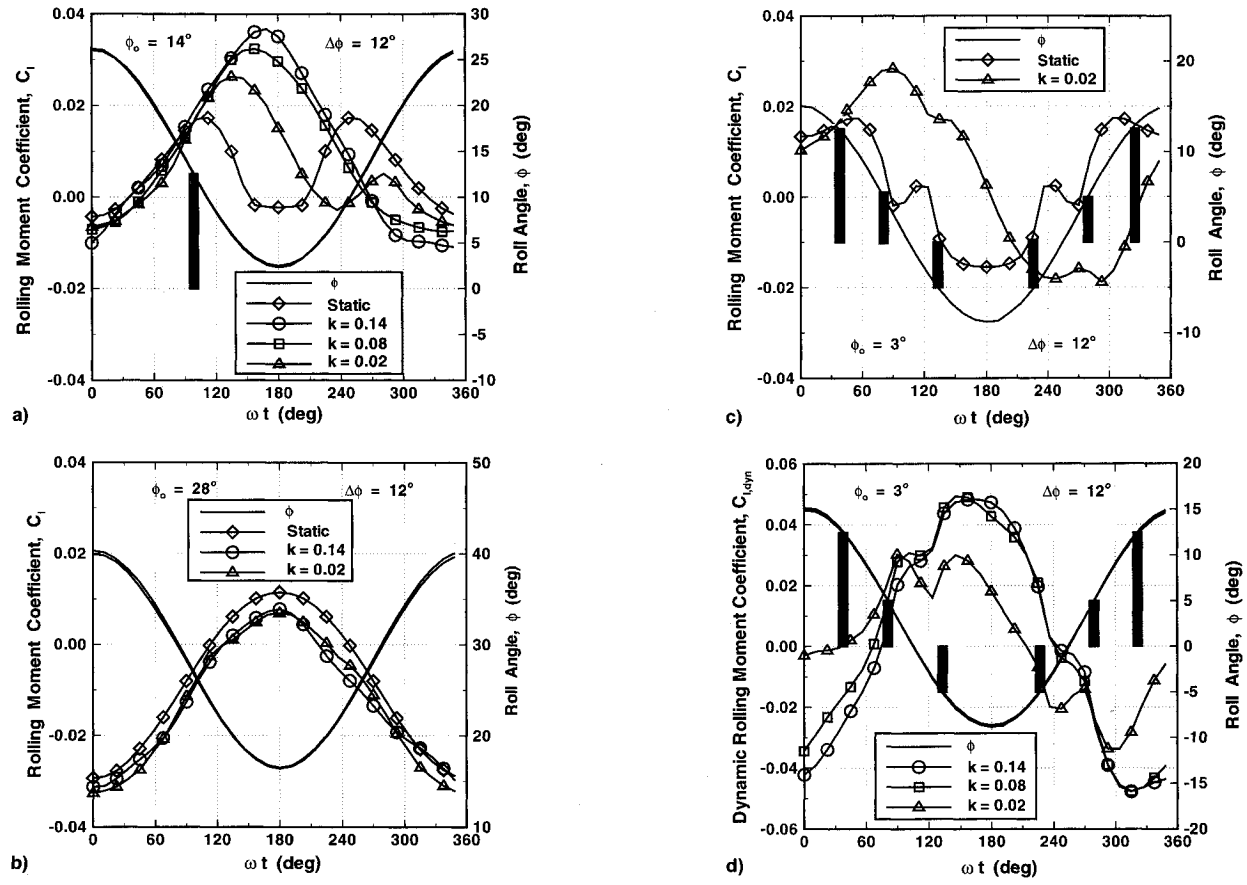

Fig. 8 Rolling-moment responses: harmonic motion, a) vertical bar denotes critical state, b) no critical state encounters, and c) vertical bars denote critical states; and d) dynamic rolling-moment responses: harmonic motion, vertical bars denote critical states.

down pitching moment increment and a positive (right wing down) rolling-moment increment as the roll angle increases from +4 to +5 deg, are consistent with the aft movement of the vortex breakdown point on the lee wing noted earlier.

Finally, as shown in Fig. 7d, considerable improvement in the polynomial fit is possible if the independent variable range is broken into regions and distinct polynomials are used for each of them. Interestingly, if breakpoints are included only at $\phi = \pm 4.5$ deg to model apparent discontinuities there, the polynomial's slope at 4.5^+ deg contrasts sharply with test data at 5, 6, and 7 deg. An additional breakpoint for the critical state at approximately 13 deg would resolve this mismatch in slopes. In summary, the inability to perform polynomial fits (without breaking the interval into smaller pieces) supports the notion that critical states exist near the locations cited previously. Again, additional static data are needed to fully justify this conclusion.

Thus, for $|\phi|$ decreasing through 5 deg (breakdown moving from the wake to a position over the wing), static flow visualization and force/moment data suggest that a change in flow topology is quickly followed by a subcritical bifurcation involving an oscillatory instability. (Chaderjian and Schiff's[22] computational results reinforce the view that there are large-scale fluctuations present in the equilibrium state.) However, as the vortex breakdown approaches the wing apex, $|\phi| \approx 13$ deg, the bifurcation that occurs would appear to be supercritical.

Dynamic Forces and Moments

If the conditions outlined, $|\phi| \simeq 5$ and 13 deg, are indeed critical states, there may be discernible transients associated with them. A previous analysis[8] of IAR data suggested that at least one of these conditions contributed to significant dynamic effects. In this section, SARL rolling-moment measurements under dynamic conditions are examined for this behavior.

Recall that the dynamic data are steady-state responses to harmonic motion, i.e., starting transients have dissipated and the aerodynamic response for each cycle is identical. Thus, if time scales appropriate for the aerodynamic response are sufficiently large compared to the period of the motion, the measured responses represent an aggregate of effects that were initiated during earlier cycles. A significant frequency effect will be observed under these conditions. Furthermore, transient responses to single events occurring at discrete points during each cycle become apparent as the frequency of the motion is decreased.

Dynamic rolling-moment data taken for a 12-deg amplitude body-axis rolling motion, centered about a mean roll angle of 14 deg, is presented in Fig. 8a. The abscissa is the argument (ωt) of the cosine function that defines the motion. Thus, precisely one cycle of motion is presented regardless of frequency. Dynamic data taken at three reduced frequencies (k = 0.02, 0.08, and 0.14, respectively), are shown. In addition, the rolling-motion time history and static data (plotted as functions of the instantaneous roll angle) are presented for reference.

Note the dramatic differences in waveform between responses at the two highest reduced frequencies and the k = 0.02 data (where distinct transients originating at critical states become more apparent). The critical-state encounter at an ωt of about 95 deg (highlighted by the vertical bar) is readily discernable. However, later in the cycle, where transient effects overlap, a positive identification of distinct events is more difficult.

Significantly, responses for all three frequencies follow the static data closely for ωt in the range 0 to about 95 deg (26 deg $\geq \phi \geq$ 13 deg), then depart from the static curve. In addition, dynamic responses at all frequencies approach the static value at the end of the cycle, the deviation increasing with frequency. Thus, the rolling-moment response appears to be essentially quasisteady when transients due to critical-state encounters have

had time to die out. This notion is supported by the data presented in Fig. 8b, which show static and dynamic rolling-moment data for 12-deg oscillations about a mean roll angle ϕ_0 of 28 deg. Roll angles traversed by this motion, 16–40 deg, preclude any encounters with suspected critical states. Differences between the static and dynamic data are likely within interpolation errors caused by the sparsely spaced static data in this region. Again, if there are no recent critical-state encounters, the rolling-moment behavior is quasisteady.

The situation shown in Fig. 8c is somewhat different; in this case, the motion (12-deg amplitude about a 3-deg offset) is centered between critical states. Therefore, the order, number, and elapsed times between encounters are different than those in Fig. 8a. Also, roll rates at $|\phi| = 5$ deg are much higher than before (the converse is true at $\phi = 12$ deg). Definite breaks in the rolling-moment response are evident at $\phi = \pm 5$ deg. Again, a departure from quasisteady behavior is seen early in the cycle (at about $\phi = 12$ deg).

When the static (equilibrium) flow is time-invariant, the NIR can be represented as the difference between its steady-state response and the deficiency function.[2,23] The deficiency function is defined as

$$F[\phi(\xi);\, t,\, \tau] = C_{l_\phi}[\phi(\xi);\, \infty,\, \tau] - C_{l_\phi}[\phi(\xi);\, t,\, \tau]$$

where, in this case, the steady-state part (first term on the RHS) is the derivative of the static rolling moment with respect to roll angle. (Also, the steady-state term on the RHS can be taken as the mean value of the static rolling-moment derivative when the equilibrium state is time dependent.)

Thus, the time-varying part of the NIR is represented by the deficiency function. When this form of the NIR is put into the superposition integral [Eq. (1)], the steady-state part integrates directly to give the change in the static coefficient between the limits of integration. Therefore, the steady-state parts of the initial condition, ΔC_l, and the two integrals, sum to the instantaneous value for the static rolling-moment coefficient $C_{l,\mathrm{stat}}[\phi(t)]$. Even in the nonlinear case, with critical states present, the total response under dynamic conditions may be separated into a static component (evaluated at the instantaneous roll angle) and a dynamic component.

The dynamic rolling moment coefficient $C_{l,\mathrm{dyn}}$ is shown in Fig. 8d for a roll-angle offset of a 3- and 12-deg amplitude (the same motion as Fig. 8c). Comparing Figs. 8c and 8d, note that the static and dynamic components are the same order of magnitude. Also, as shown in Fig. 8d, locations for critical states, identified from both static flowfield structure and static force behavior, correlate well with dramatic changes in the dynamic rolling-moment response.

The results discussed earlier for a limited number of motions apply over a wide range of test conditions as shown in Figs. 9a–9c. Each of these is a contour plot of the dynamic (total minus static) rolling-moment coefficient presented in the phase plane. Each represents $k = 0.08$ data for the complete range of test amplitudes at a given roll-angle offset. A series of tests with fixed offset and frequency generates a family of ellipses, centered about the offset angle. As the rolling motion proceeds, the ellipses are traversed in the clockwise direction. Offsets for each of the figures are 0, 7, and 14 deg, respectively.

The contours were established by first finding a mathematical representation for the rolling-moment data. A regression procedure, similar to that reported in Ref. 8, was used to do this. A correlation coefficient of 0.97 was achieved for data covering all test conditions at $k = 0.08$ and 0.14.

In all cases presented in Figs. 9a–9c, the contour lines turn rapidly, becoming essentially parallel to the roll-rate axis at $\phi = \pm 5$ deg. Moving clockwise in the bottom half of the ellipse through $\phi = -5$ deg, the contour lines again turn rapidly between -10 and -15 deg to run nearly parallel to the roll angle axis. Note that this turning point is less distinct than the first, perhaps because the static data have been faired

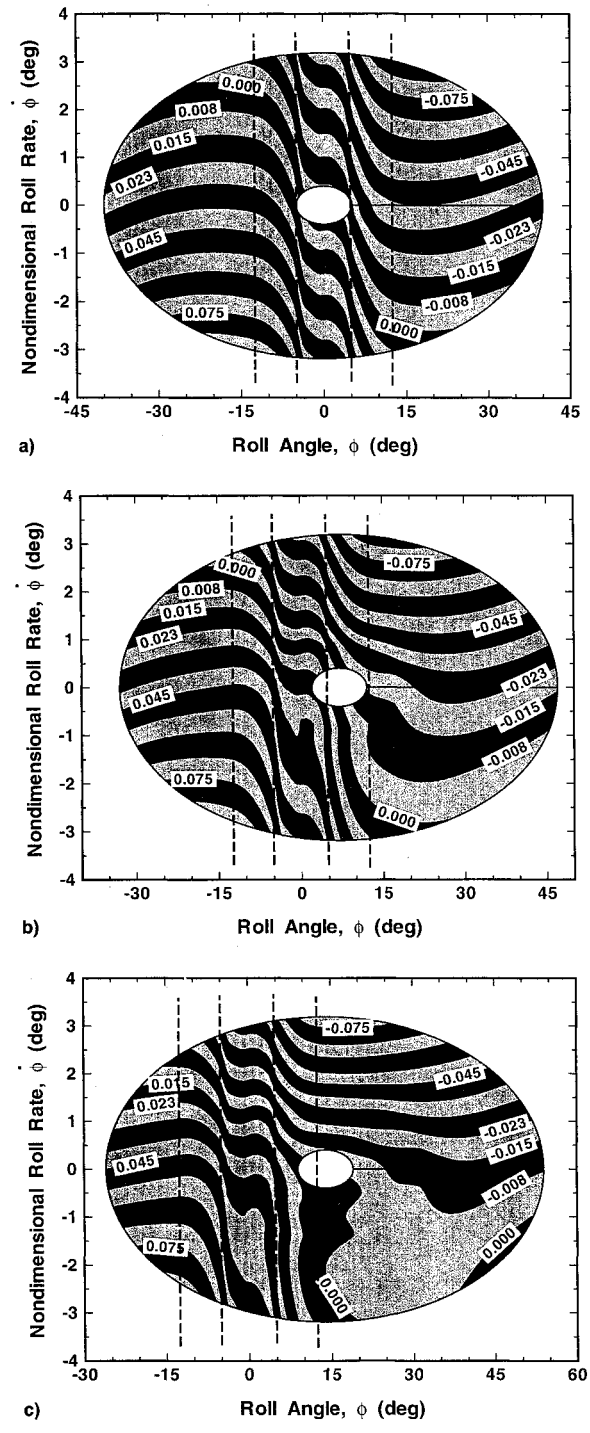

Fig. 9 Dynamic rolling-moment contours: a) $k = 0.08$, $\phi_0 = 0$ deg; b) $k = 0.08$, $\phi_0 = 7$ deg; and c) $k = 0.08$, $\phi_0 = 14$ deg.

through this region. The pattern repeats in the upper half of the figure. Significantly, the loci of turning points are independent of roll rate, further evidence that they are critical states because they are determined by equilibrium conditions.

Following a critical-state encounter, the dynamic response becomes weakly dependent on roll angle (contour lines nearly parallel to the roll-angle axis). Contours in this region are likely the result of expressing time variations implicitly in the phase plane (rather than an actual dependence on roll angle or roll rate).

Finally, note that as the offset roll angle is increased (allowing more time to elapse between the critical-state encounter near 13 deg with positive roll rate and the next 13-deg critical-state encounter with negative roll rate) the region of negligible

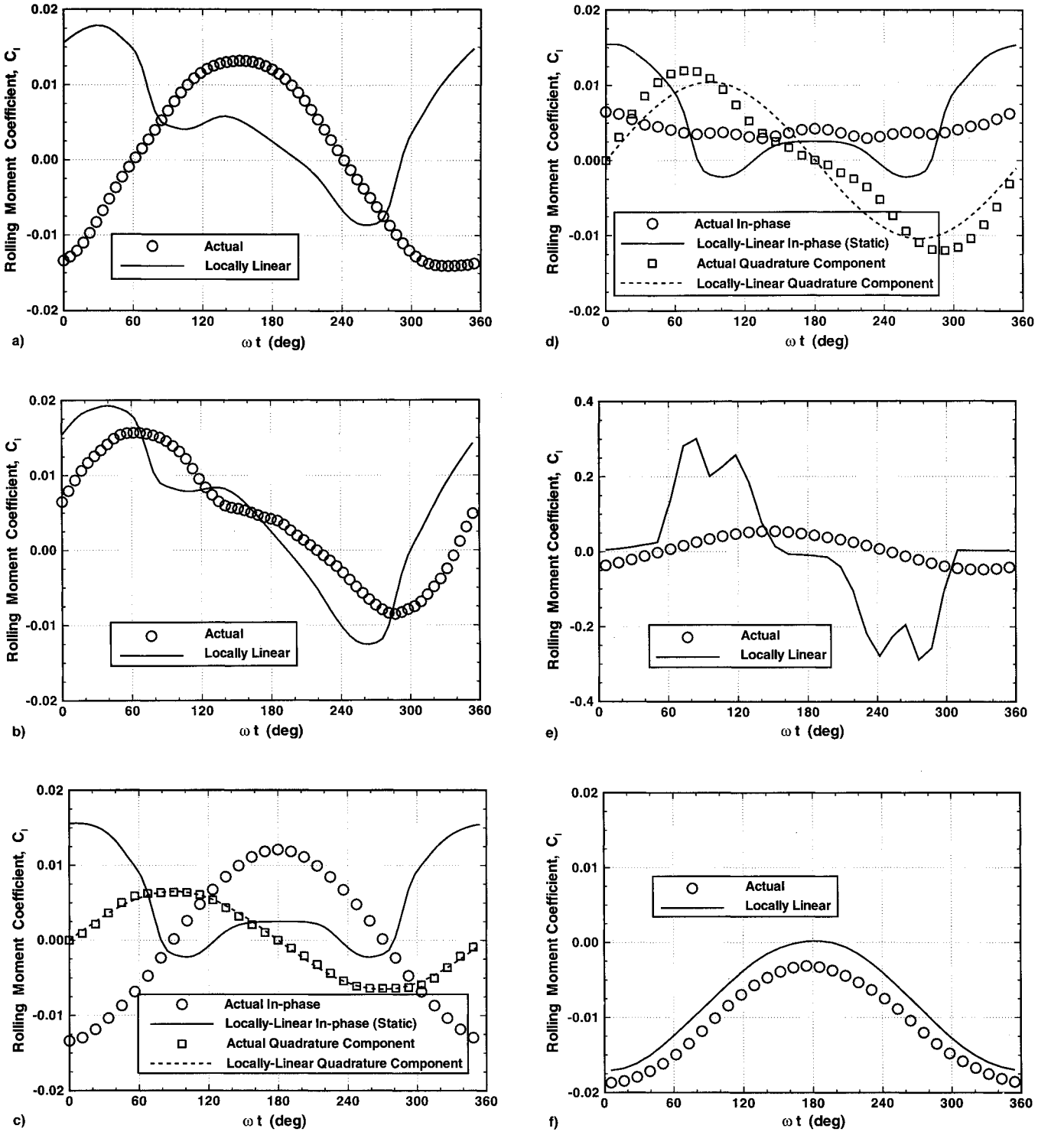

Fig. 10 Comparison between actual data and locally linear model: a) $k = 0.14$, $\phi_0 = 3$ deg, and $\Delta\phi = 5$ deg and b) $k = 0.02$, $\phi_0 = 3$ deg, and $\Delta\phi = 5$ deg; in-phase and quadrature component comparisons: c) $k = 0.14$, $\phi_0 = 3$ deg, and $\Delta\phi = 5$ deg and d) $k = 0.02$, $\phi_0 = 3$ deg, and $\Delta\phi = 5$ deg; e) effect of extrapolating low-frequency derivatives to high rates, $k = 0.14$, $\phi_0 = 3$ deg, and $\Delta\phi = 18$ deg; and f) locally linear model vs actual data: no critical states, $k = 0.14$, $\phi_0 = 28$ deg, and $\Delta\phi = 5$ deg.

dynamic rolling moment in the lower-right quadrant expands. There is more time for the transient to decay.

Significance of Results

Locally linear models are often used to represent aerodynamic forces and moments in nonlinear flight simulations. In this model, static forces and moments are represented by nonlinear functions of instantaneous values of angle of attack and sideslip. Dynamic effects are calculated by using locally linear damping derivatives (linearized about the instantaneous vehicle state). Dynamic nonlinearities are accounted for by allowing derivatives to be functions of angle of attack and sideslip.

Linearization of the damping derivatives is often a consequence of the testing technique used to measure them. Small-amplitude harmonic vehicle motions are used and only the quadrature component of the loads at the frequency of the oscillation is considered. Although this procedure is acceptable in the absence of significant nonlinearities (as is the case in many small amplitude motions), it leads to results that cannot,

in general, be legitimately extrapolated in terms of rate, which is precisely what locally linear models do.

To check the validity of locally linear damping derivatives in the current case, forced oscillation data were reduced in this manner, i.e., nonlinear static rolling-moment data were used together with roll-damping derivatives, obtained from 5-deg amplitude tests at different offset angles.[10] Only the out-of-phase rolling moment at the forcing frequency was retained, although up to 20 harmonics were recorded. Thus, the result is a derivative linearized about the mean roll angle of the motion. The locally linear model was then used to predict the measured rolling moment (with all harmonics) over the same motion as used to determine the damping derivative.

Comparisons between the model and measured responses are shown in Figs. 10a–10f. In Figs. 10a–10d and 10f, the damping derivative is taken to be constant (consistent with the small amplitude, 5 deg, over which it was determined). However, in Fig. 10e the damping derivative was represented by a nonlinear function of roll angle (owing to the larger amplitude, 18 deg).

Figures 10a and 10b show results for $\phi_0 = 3$ deg and reduced frequencies of $k = 0.14$ and 0.02, respectively. The correlation presented in Fig. 10a is totally unacceptable. Over much of the cycle, the model predicts a positive rolling moment, while the actual response is the opposite. At the lowest reduced frequency ($k = 0.02$ in Fig. 10b), there is much better agreement, but the result is still inadequate. Even at this extremely low reduced frequency, there is a lag in the actual response that is not captured by the locally-linear model.

Further insight is provided by Figs. 10c and 10d, which should be compared to Figs. 10a and 10b, respectively. In-phase (circular symbols) and quadrature (squares) components of the actual responses are compared to the corresponding components according to the locally-linear model; i.e., static rolling moment and linearized damping terms, respectively. At $k = 0.14$, linearization of the damping term (based on experimental data taken at this frequency) is certainly valid over the range of roll rates encountered in Fig. 10c. However, significant errors are introduced by approximating the in-phase component with the static data.

Similarly, at $k = 0.02$, most of the locally linear model's error is again seen to be due to a poor prediction of the in-phase component as shown in Fig. 10d. However, some nonlinear effects are now seen in the quadrature component. The latter problem is compounded if damping derivatives based on small-amplitude, low-frequency ($k = 0.02$) data are used to extrapolate to higher angular rates. Such a case is shown in Fig. 10e where the prediction for $k = 0.14$ with 3-deg offset and 18-deg amplitude is compared with the corresponding observed rolling moment. Note that the 5-deg amplitude, the smallest used in this test series, is two to three times larger than that used in typical low-amplitude tests. Derivatives based on larger amplitude data (with their associated higher rates) can therefore be expected to yield better predictions when extrapolated to the high rates. Even so, the results are totally unacceptable; the in-phase component errors are completely swamped by those in the damping term. Note that the peaks in the prediction are centered about ωt values of 90 and 270 deg where the rate is the highest.

Finally, note the good agreement in Fig. 10f. In this case, the offset roll angle of 28 deg and the 5-deg amplitude ensure that the critical states cannot be reached. The discrepancies here are likely the result of interpolation errors in the static component. Thus, the principal difficulty with the locally linear model noted here is when the motion includes critical states.

Similar effects can be observed in Fig. 11 where trajectories corresponding to three free-to-roll releases are superimposed on a phase-plane portrait constructed with the locally linear model. Obviously the latter is totally incapable of representing the dramatic motion history effects and nonlinearities that prevail following critical-state encounters. Therefore, testing techniques must involve model motions capable of eliciting the transient responses not observable with small-amplitude low-rate experiments. Instantaneous values for aerodynamic loads must be measured to permit observations of these transients. Furthermore, changes in skin-friction and flowfield topology (together with a careful interpretation of static data) may indicate values for flow and motion parameters where critical states are likely to occur.

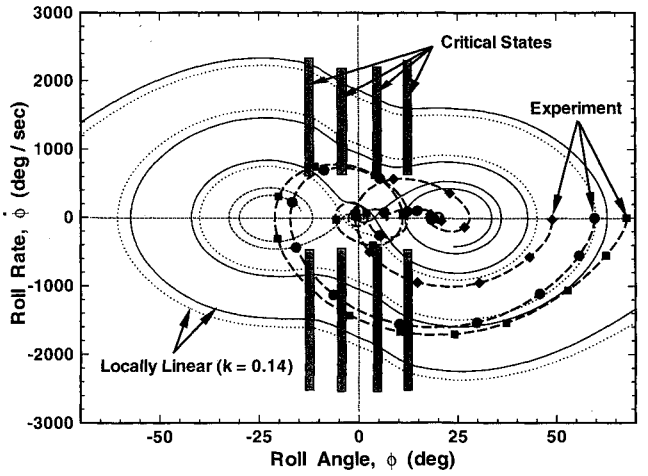

Fig. 11 Actual free-to-roll motions vs locally linear phase portrait.

Clearly, significant errors result if the effects of critical-state encounters are not handled correctly. Therefore, aerodynamic models that can account for the existence of critical states and the transients induced by them are required.

Acknowledgments

This work was conducted under a Joint Research Program of the U.S. Air Force Office of Scientific Research, Wright Laboratory, the Institute for Aerospace Research, and the Canadian Department of National Defence. The support of these organizations is gratefully acknowledged. The authors are also indebted to Murray Tobak whose counsel (particularly regarding the effects of time-averaged data on the analysis) was indispensable to the interpretation and presentation of these results.

References

[1]Tobak, M., Chapman, G. T., and Unal, A., "Modeling Aerodynamic Discontinuities and Onset of Chaos in Flight Dynamical Systems," *Annales des Telecommunications*, Tome 42, Nos. 5 and 6, 1987, pp. 300–314; also NASA TM-89420, Dec. 1986.

[2]Tobak, M., Chapman, G. T., and Schiff, L. B., "Mathematical Modeling of the Aerodynamic Characteristics in Flight Mechanics," *Proceedings of the Berkeley–Ames Conference on Nonlinear Problems in Control and Fluid Dynamics*, Math Sci Press, Brookline, MA, 1985, pp. 435–450; also NASA TM-85880, Jan. 1984.

[3]Tobak, M., and Chapman, G. T., "Nonlinear Problems in Flight Dynamics Involving Aerodynamic Bifurcations," *AGARD Symposium on Unsteady Aerodynamics—Fundamentals and Applications to Aircraft Dynamics*, CP-386, AGARD, 1985, pp. 25-1–25-15.

[4]Tobak, M., and Unal, A., "Bifurcations in Unsteady Aerodynamics," NASA TM-88316, June 1986.

[5]Truong, K. V., and Tobak, M., "Indicial Response Approach Derived from Navier-Stokes Equations: Part 1—Time-Invariant Equilibrium State," NASA TM-102856, Oct. 1990.

[6]Hanff, E. S., "Dynamic Nonlinear Airloads—Representation and Measurement," *AGARD Symposium on Unsteady Aerodynamics—Fundamentals and Applications to Aircraft Dynamics*, CP 386, AGARD, 1985, pp. 27-1–27-14.

[7]Hanff, E. S., "Large Amplitude Oscillations," *Special Course on Aircraft Dynamics at High Angles of Attack: Experiments and Modelling*, AGARD Rept. 776, 1991, pp. 4-1–4-19.

[8]Jenkins, J. E., and Hanff, E. S., "Non-Linear Airloads Hypersur-

face Representation—A Time Domain Perspective," *Manoeuvring Aerodynamics*, CP 497, AGARD, 1991, pp. 7-1–7-9.

[9]Hanff, E. S., Kapoor, K., and Anstey, C. R., "Large-Amplitude High-Rate Roll Oscillation System for the Measurement of Non-Linear Airloads," AIAA Paper 90-1426, 1990.

[10]Hanff, E. S., and Jenkins, S. B., "Large-Amplitude High-Rate Roll Experiments on a Delta and Double-Delta Wing," AIAA Paper 90-0224, Jan. 1990.

[11]Hanff, E. S., and Ericsson, L. E., "Multiple Roll Attractors of a Delta Wing at High Incidence," *AGARD Symposium on Vortex Flow Aerodynamics*, CP 494, AGARD, 1990, pp. 31-1–31-10.

[12]Hanff, E. S., and Huang, X. Z., "Roll-Induced Cross-Loads on a Delta Wing at High Incidence," AIAA Paper 91-3223, Sept. 1991.

[13]Arena, A. S., Jr., Nelson, R. C., and Schiff, L. B., "An Experimental Study of the Nonlinear Dynamic Phenomenon Known as Wing Rock," *AIAA Atmospheric Flight Mechanics Conference*, AIAA, Washington, DC, 1990, pp. 173–183 (AIAA Paper 90-2812).

[14]Sattinger, D. H., "Bifurcation and Symmetry Breaking in Applied Mathematics," *Bulletin (New Series) of the American Mathematical Society*, Vol. 3, No. 2, 1980, pp. 779–819.

[15]Tobak, M., and Peake, D. J., "Topology of Three-Dimensional Separated Flows," *Annual Review of Fluid Mechanics*, Vol. 14, 1982, pp. 61–85.

[16]Dennis, S. C. R., and Chang, G., "Numerical Solutions for Steady Flow Past a Cylinder at Reynolds Numbers up to 100," *Journal of Fluid Mechanics*, Vol. 42, Pt. 3, 1970, pp. 471–489.

[17]Nishioka, M., and Sato, H., "Mechanism of Determination of the Shedding Frequency of Vortices Behind a Cylinder at Low Reynolds Numbers," *Journal of Fluid Mechanics*, Vol. 89, Pt. 1, 1978, pp. 49–60.

[18]Chen, J.-H., Pritchard, W. G., and Tavener, S. J., "Bifurcation for Flow Past a Cylinder Between Parallel Planes," *Journal of Fluid Mechanics*, Vol. 284, Feb. 1995, pp. 23–41.

[19]Wentz, W. H., and Kohlman, D. L., "Vortex Breakdown on Slender Sharp-Edged Delta Wings," AIAA Paper 69-778, July 1969.

[20]Payne, F. M., and Nelson, R. C., "An Experimental Investigation of Vortex Breakdown on a Delta Wing," *Vortex Flow Aerodynamics—Vol. I*, 1985, pp. 135–161 (NASA CP 2416).

[21]Conte, S. D., *Elementary Numerical Analysis*, McGraw–Hill, New York, 1965, p. 140.

[22]Chaderjian, N. M., and Schiff, L. B., "Navier-Stokes Prediction of a Delta Wing in Roll with Vortex Breakdown," AIAA Paper 93-3495, Aug. 1993.

[23]Jenkins, J. E., "Simplification of Nonlinear Indicial Response Models: Assessment for the Two-Dimensional Airfoil Case," *Journal of Aircraft*, Vol. 25, No. 2, 1991, pp. 131–138.